S. J. Pennycook[a,b], A. R. Lupini[a], A. Kadavanich[a,c*], J. R. McBride[c], S. J. Rosenthal[b,c], R. C. Puetter[d], A. Yahil[d], O. L. Krivanek[e], N. Dellby[e], P. D. L. Nellist[e], G. Duscher[a,f], L. G. Wang[a#], S. T. Pantelides[a,b]

[a] Solid State Division, Oak Ridge National Laboratory, Oak Ridge, TN, USA
[b] Department of Physics and Astronomy, Vanderbilt University, Nashville, TN, USA
[c] Department of Chemistry, Vanderbilt University, Nashville, TN, USA
[d] Pixon LLC, 11 Night Heron Drive, Stony Brook, NY, USA
[e] Nion Co., Kirkland, WA, USA
[f] Department of Materials Science and Engineering, North Carolina State University, Raleigh, NC
* Now at Mattson Technology, Fremont, CA, USA
# Now at National Renewable Energy Laboratory, Golden, CO, USA

Aberration-corrected scanning transmission electron microscopy: the potential for nano- and interface science

Dedicated to Professor Dr. Dr. h. c. Manfred Rühle on the occasion of his 65th birthday

The sub-Ångström probe of an aberration-corrected scanning transmission electron microscope will enable imaging and analysis of nanostructures and interfaces with unprecedented resolution and sensitivity. In conjunction with first-principles theory, new insights are anticipated into the atomistic processes of growth and the subtle link between structure and functionality. We present initial results from the aberration-corrected microscopes at Oak Ridge National Laboratory that indicate the kinds of studies that will become feasible in the near future. Examples include (1) the three-dimensional location and identification of individual dopant and impurity atoms in semiconductor interfaces, and their effect on local electronic structure; (2) the accurate reconstruction of surface atomic and electronic structure on nanocrystals, and the effect on optical properties; and (3) the ability to distinguish which configurations of catalyst atoms are active, and why.

Keywords: Scanning transmission electron microscopy; *Z*-contrast; Aberration correction; Nanoscience

1. Introduction

Scanning transmission electron microscopy (STEM) allows simultaneous *Z*-contrast imaging and electron energy loss spectroscopy (EELS) with the resolution of the probe, as shown in Fig. 1 [1]. Nowadays, commercial microscopes routinely provide electron beams of atomic dimensions coupled with efficient parallel detection electron energy loss spectrometers [2]. In the STEM, imaging is achieved using a highly coherent probe which is scanned across the specimen. The intensity reaching some detector is then used to form an image. The detector plane contains a coherent diffraction pattern with a large amount of detailed structure. However, since interference *redistributes* intensity in the detector plane, while conserving the total intensity, the essential requirement for incoherent imaging is that the detector *integrates* sufficient details of the interference pattern [3, 4]. With a high-angle annular dark-field detector, and a large spectrometer entrance aperture, both will give incoherent images with a simple and direct correlation with each other, and with the specimen. In the case of a zone-axis

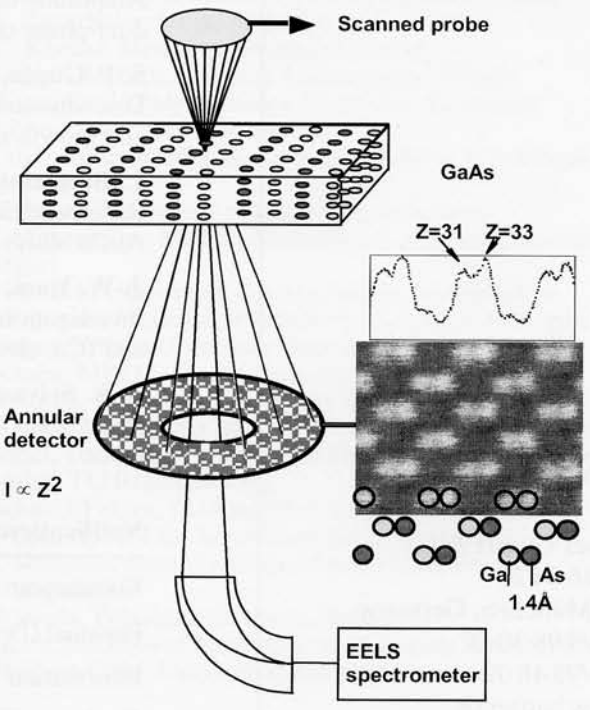

Fig. 1. Schematic showing simultaneous *Z*-contrast imaging and EELS in the STEM. The image, taken with the uncorrected VG Microscopes 603U STEM, distinguishes the sublattice polarity in GaAs; *Z* = atomic ordernig number.

crystal, this extends even to the atomic scale; the STEM probe can be located on an *individual* atomic column selected from the image for EELS measurements of local concentration and electronic structure [5–7].

Experimentally, these images show all the characteristics of an incoherent, column-by-column image: intuitive dependence on objective lens focus and specimen thickness, no Fresnel fringes at interfaces or delocalized lattice planes around nanocrystals, a *Z*-contrast image with localization apparently limited only by the shape of the probe itself. However, it is far from immediately obvious how this can be true. How can column-by-column imaging and analysis be possible in the presence of dynamical diffraction and broadening of a highly convergent incident probe? Calculations of the intensity distribution inside a crystal will suggest a focused probe spreads over many lattice sites. But the intensity inside the crystal is not a quantum mechanical observable – only the intensity reaching a detector [8]. A Bloch wave analysis shows that the reason for the localized, intuitive nature of the *Z*-contrast image is because a *high-angle* annular dark field (HAADF) detector detects only *localized* states in the crystal, 1s type Bloch states [9, 10]. A similar analysis explains column-by-column EELS. Although less localized than the HAADF detector, with a *large* spectrometer acceptance aperture it is still sufficiently local to provide an incoherent, column-by-column image [11]. In contrast, the small axial detector needed for coherent bright-field imaging accepts contributions from all states, which can result in a non-local image and interference effects.

Furthermore, the high-angle scattering is largely quasi-elastic, it has been scattered by phonons. The presence of this diffuse scattering in the exit face wave function leads to an effective thickness integration; in contrast the bright field detector analyses the low angle components of the exit face wave function, resulting in an image that is predominantly coherent. In the limit of high thickness, the incoherent HAADF image approximates to a convolution between the probe intensity profile and a columnar object function proportional to Z^2. In thinner crystals, the effective thickness integration means that HAADF images carry information on specimen thickness, with the potential to extract three-dimensional information. At low resolution, tomographic reconstruction has already been demonstrated [12, 13]. It should be noted that other contrast mechanisms can also be important: diffraction contrast gives contrast from crystal defects just as in bright field images, although the contrast differs in form [14]. Variations in the thermal vibration amplitude or static strains also can give strong image contrast [15].

The feasibility of correcting the inherently large spherical aberration of microscope objective lenses promises to revolutionize the field of microscopy and microanalysis [16, 17]. The potential benefits for STEM imaging may turn out to be much greater than those for the conventional imaging because it is very much less sensitive to instabilities [18]. Furthermore STEM would seem to be the only viable route to the analysis of individual atoms and their local electronic environment. The correction of objective lens aberration is achieved through a set of multipole lenses that produce a negative spherical aberration (C_s) to cancel the inherently large positive C_s of the conventional round objective lens. Computer diagnosis and correction of aberrations then enables the probe-forming aperture to be enlarged to produce a smaller probe. It is now possible to more than double the resolution of these microscopes [19].

Even without aberration-corrected beams, the combination of atomic-resolution *Z*-contrast microscopy, electron energy loss spectroscopy and first-principles theory has proved to be a powerful means for structure property correlations at interfaces [20–23]. The *Z*-contrast image has revealed atomic arrangements both at isolated dislocation cores [24], and at dislocation arrays that comprise grain boundaries [25, 26]. Some of these atomic configurations have been unexpected, but could be rationalized by theory [18]. Performing structural relaxations of configurations suggested from experiment is highly efficient, both computationally and experimentally. It avoids the need to calculate the large number of potential defect configurations, the number of which increases enormously as the system complexity increases. Experimental atomic positions are also not required to especially high accuracy. Theory can both confirm and refine the structure suggested from the image, or choose between different possible structures with similar projections on the basis of total energies. Segregation energies, local electronic structure and optical properties can all be calculated [27, 28].

2. Initial results from the ORNL 100 kV aberration-corrected STEM

The 100 kV VG Microscopes HB501UX at Oak Ridge National Laboratory (ORNL) has recently been fitted with an aberration corrector constructed by Nion Co., which improved its resolution from 0.22 nm (full-width-half-maximum probe intensity at Scherzer defocus) to approximately 0.1 nm. It now has better performance than the uncorrected *300 kV* HB603U STEM at ORNL with a directly interpretable resolution of 0.13 nm. Although this microscope has demonstrated information transfer down to 0.078 nm, this was achieved using an oversized objective aperture and large defocus causing very extended probe tails and weak image contrast [13]. An aberration corrector has now been installed which is predicted to bring the directly interpretable resolution down to 0.05 nm with a highly localized probe and strong image contrast. At the time of writing this microscope is limited to a resolution of ≈ 0.09 nm due to instabilities. Figure 2 demonstrates the improved performance of the ORNL STEMs. Care was taken to avoid artifacts in the Fourier transforms which can lead to spurious weak high frequency spots. In all cases the envelope of the spots is consistent with the smoothly decreasing transfer function expected for incoherent imaging.

Figure 3 shows the sensitivity to single atoms available with the enhanced resolution of the 100 kV STEM. Single Bi atoms are visible within a Si crystal and intensity profiles across the image reveal which of the two columns of the dumbbell contain the Bi atom. Results are comparable to those recently obtained with a 200 kV STEM [29]. The density of bright spots correlates with the known concentration of Bi, which was introduced by ion implantation followed by recrystallization through solid phase epitaxial growth. This procedure placed 93 % of the Bi atoms on substitutional sites. The cross-section sample was prepared by standard ion milling procedures using a final cleaning at 0.5 kV.

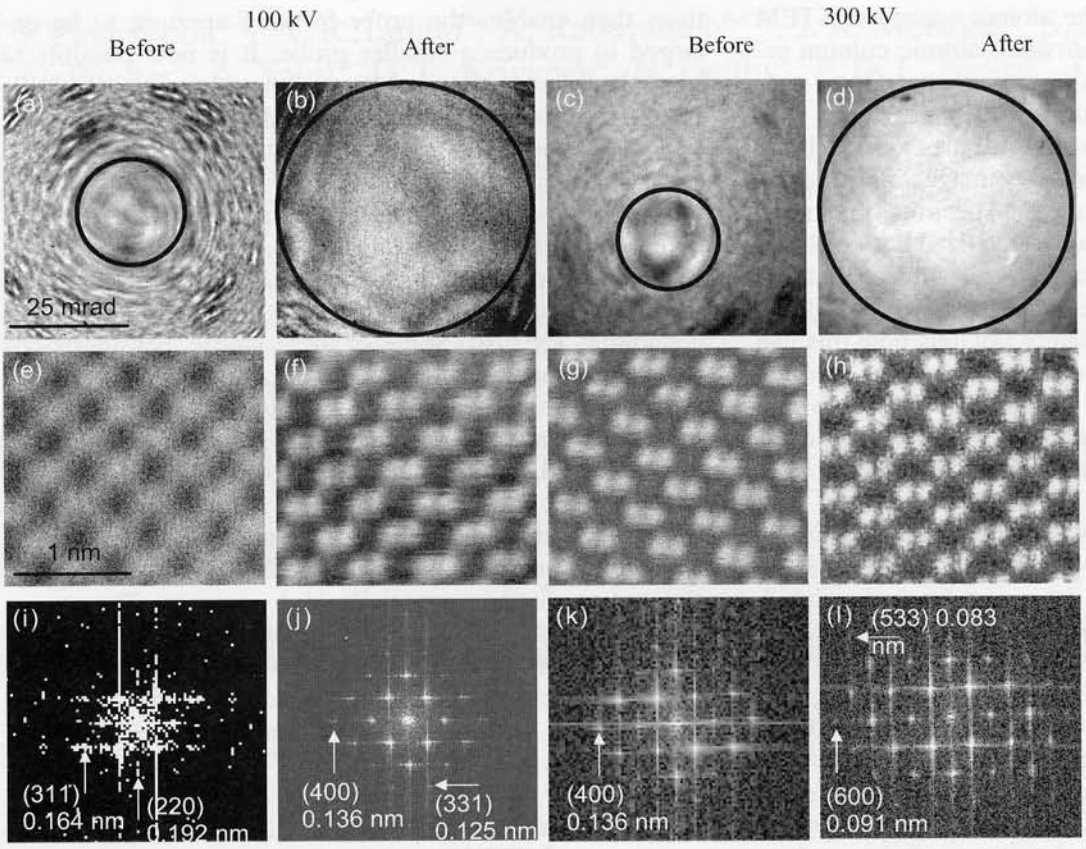

Fig. 2. Ronchigrams observed in far-field with the probe stationary on the sample

(a) for the 100 kV microscope before autotuning
(b) after aberration correction
(c) for the uncorrected 300 kV microscope
(d) after aberration correction. In both cases, the extent of uniform phase has increased about 2.5 times. Images of Si ⟨110⟩ show the improvement in image resolution from
(e) 0.19 nm to
(f) 0.13 nm on the 100 kV microscope, and from
(g) 0.13 nm to
(h) 0.09 nm on the 300 kV microscope.

The thickness on this region was estimated at 300 Å, a little more than one extinction distance of the 1s Bloch state responsible for the image. In this case, a single atom will show depth dependent contrast due to the periodic nature of the dynamical wave field. The histogram of the Bi atom contrast in Fig. 3 shows the variability of the contrast. A channeling model provides an approximate analytical description of the process: the dynamical wave field is modeled as two components, the 1s state propagating with its specific wave vector and everything else propagating at a different wave vector [30–32]. The justification for this simplified model is that the 1s states are the most strongly bound eigenstates and are the first therefore to acquire a significant phase difference. Interference between the two clusters predicts the depth dependent dynamical wave field contributing to the detected intensity, as shown in Fig. 4. A single Bi atom will scatter proportional to the dynamical wave field at its *specific* depth in the crystal. For a sufficiently high angle detector, the signal scattered by the Si matrix is predominantly diffuse scattering, which leads to an effective thickness integration as mentioned before. Column-by-column imaging, therefore, does not sample all atoms in the column equally, and this can be exploited to provide depth information on single atom impurities or dopants. In a crystal matrix half an extinction distance in thickness, the intensity of a Bi atom will give a direct indication of its depth.

Figure 5 shows a *Z*-contrast image of a Si/SiO_2 interface, a line scan of the image intensity with EELS spectra recorded simultaneously. The bright region near the interface is due to random static strains. These increase the total Debye-Waller factor and give a greater detected intensity for certain detector angles [3]. The geometric roughness is of the interface is seen to be $\approx 4-5$ Å. In contrast, the EELS spectra show that the electronic effect of the interface extends *significantly further* than the geometric extent. The EELS edge takes ≈ 1 nm for the transition from bulk Si, which shows a Si $L_{2,3}$ edge onset at ≈ 100 eV, to full stoichiometric SiO_2 with an edge onset at 106 eV. This is not due to delocalization of the inelastic scattering [33]; calcu-

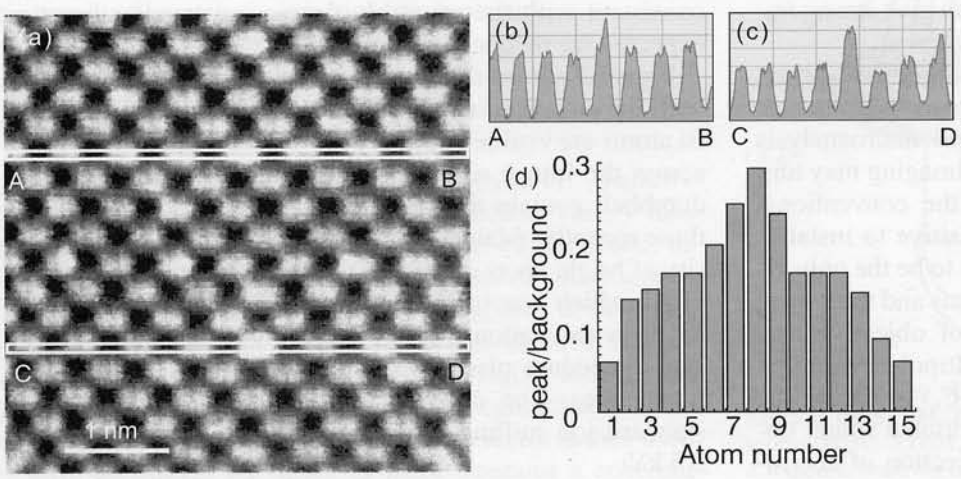

Fig. 3. *Z*-contrast image of Bi-doped Si ⟨110⟩ revealing the columns containing individual Bi atoms. The upper intensity profile shows a Bi atom on the right hand column of a Si dumbbell, the lower profile shows a Bi atom in each of the two columns of a dumbbell.

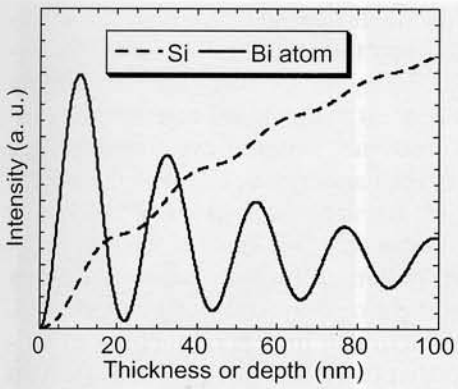

Fig. 4. Approximate form of the image intensity from Si with thickness (broken line) and of the intensity scattered by single substitutional Bi atom as a function of depth within the crystal, calculated with a channeling model for a 100 kV incident beam incident on ⟨110⟩ Si, a 1s state extinction distance of 22 nm, a 1s state absorption coefficient of 0.01 nm^{-1} and a plane wave absorption coefficient of 0.001 nm^{-1}.

lations that avoid use of the dipole approximation show that under incoherent conditions (a large acceptance angle into the spectrometer) the ultimate EELS spatial resolution is comparable to the geometric size of the initial inner shell orbital [34–36]. In a crystal, the resolution is limited by either the probe or the 1s Bloch states, but all of these dimensions are much smaller than the effects seen here.

The spectrum from the interface is generally not a simple sum of the Si and SiO_2 but shows intensity in the region of the SiO_2 bandgap. This is due to suboxide bonds. Interpretation of these EELS spectra is possible using the same density-functional codes used for total energy calculations of

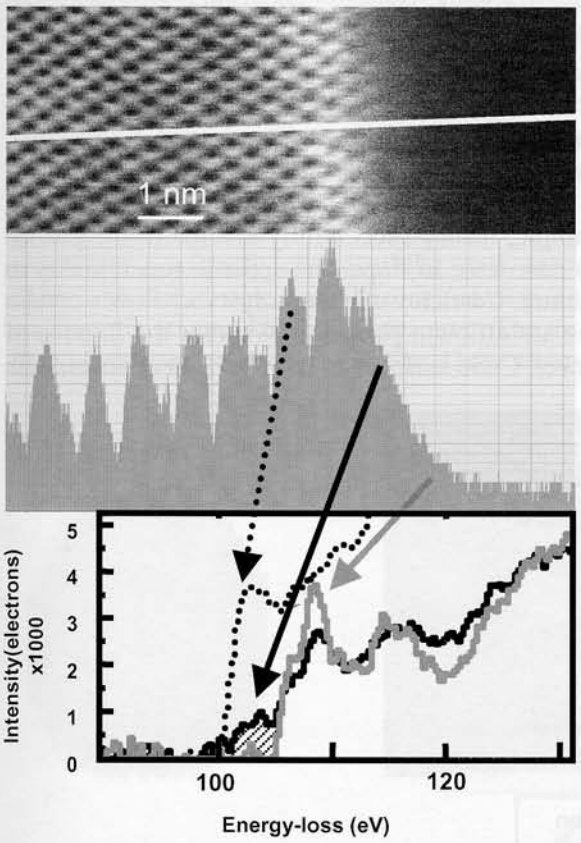

Fig. 5. Z-contrast image (top) of an irradiated and annealed Si/SiO_2 interface showing the position of a line scan for EELS. The Z-contrast intensity recorded during the line scan shows the probe position of each EELS spectrum. Three representative spectra are shown, from the Si (dotted), the interface (solid black) and stoichiometric SiO_2 (grey). Shaded region on the interface spectrum indicates suboxide bonding.

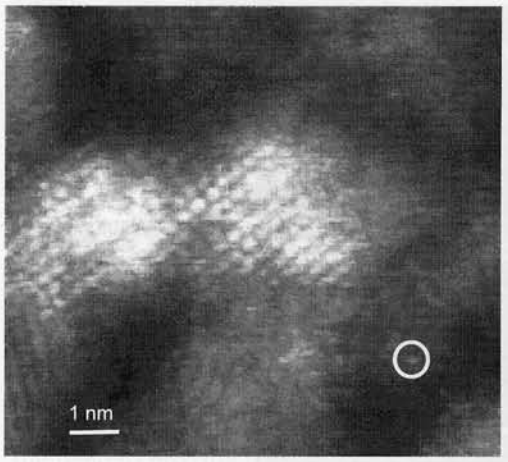

Fig. 6. Image of CdSe/ZnS core/shell nanocrystals embedded in MEH-PPV polymer. Isolated bright spots such as the one circled may correspond to single atoms.

structures, provided the effects of the core hole are included [37–40]. Although the energy threshold cannot be calculated to sufficient accuracy to compare with experiment, the shape of the near edge structure is given to good accuracy. Calculations for different possible local bonding configurations such as suboxide intrusions or an abrupt interface can be compared to experiment.

Figure 6 shows an image of small CdSe/ZnS core/shell nanocrystals synthesized by Quantum Dot Corporation using standard methods [41]. The nanocrystals were mixed with a poly-3-hexylthiophene polymer solution and spin coated onto single-crystal NaCl. Dissolving the NaCl in water, the polymer film could be picked up with lacey carbon-coated copper grids. The low density, semiconducting, polymer matrix was intended to reduce background effects and minimize contamination effects compared to nanocrystals supported on a pure carbon film. Unfortunately, variations in polymer thickness and nanocrystal aggregation tended to out-weigh these benefits. In the raw Z-STEM image, the core is seen as a bright region in the center and the shell is seen as a less bright region around it. Quality and coverage of the shell and location of the core relative to the shell, two properties which might influence the fluorescence quantum efficiency, can be easily determined. The bright dot visible in the circle may be a single atom, and shows the greatly improved sensitivity of the aberration-corrected microscope. Addition of a cathodoluminescence detector would enable the effectiveness of the passivating shell to be determined nanocrystal by nanocrystal.

3. Reconstruction of nanocrystal shape

Nanocrystals are three-dimensional objects, and their properties will depend on their exposed facets, their surface termination, the presence of interfacial defects between a core and a shell, and the electronic structure of each interface. In catalysis, the same issues are important. Active sites may turn out to be specific atomic configurations at facet junctions or surface vacancies. Although theory is an important contributor to such understanding, as we show below, it is important to extract as much information on the three-dimensional structure as possible. Figure 7 shows an image of a CdSe nanocrystal taken on the uncorrected 300 kV STEM. The projected shape is clear from the image, while

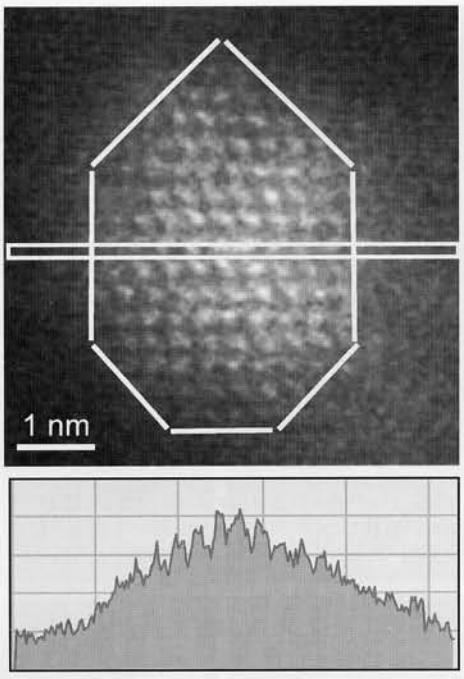

Fig. 7. Image of a well-facetted CdSe nanocrystal embedded in MEH-PPV polymer revealing projected shape, with intensity profile containing thickness information.

the intensity profiles contain information on the thickness of the nanocrystal (as expected from Fig. 4). However, the facet structure is not apparent from the raw intensities because the image contrast is rather weak. This is due both to the finite size of the probe and also because the nanocrystal is embedded in a polymer film which broadens the probe before it reaches the nanocrystal. Because the *Z*-contrast image is an incoherent technique, a convolution of the object with a resolution function, these effects can be remedied through the various image reconstruction or deconvolution techniques developed for light optical imaging. Figure 8 shows the variety of techniques that are available, which split broadly into direct methods (such as smoothing or Fourier filtering) and indirect methods which are significantly more powerful and robust to noise.

A comparison of a simple Fourier filter with the maximum entropy [42–44] and Pixon methods [45] is shown in Fig. 9. The Fourier filter improves contrast but introduces substantial spurious detail. It also has removed the thickness information. Although this could be retained, for example with a Wiener filter, direct methods that simply change the frequency content in the image can introduce artifacts [34]. Both indirect methods retrieve the sublattice polarity in the center of the nanocrystal, showing the brighter Cd columns ($Z = 48$) towards the bottom of the image with the lighter Se columns ($Z = 34$) towards the top. However, in the amorphous polymer film the maximum entropy method insists on placing a random array of point sources. This illustrates the problem that in general there is an infinite number of objects that fit a given image. The maximum entropy object can show spurious detail because it does not adjust the information content of the image locally, but treats only the entropy of the entire image. The Pixon method, however, does take into account the local image statistics, and if there is no information in the image it gives a uniform reconstruction. This makes it easier to determine the edge of the nanocrystal, while the method still extracts the nanocrystal polarity in the center.

It is not possible to reconstruct the nanocrystal shape from thickness measurements in a single projection without some additional assumption. Here, we assume that the top and bottom surfaces are symmetric. Plotting the columnar intensities top to bottom, and left to right, the thickness profile of the nanocrystal becomes clearer (Fig. 10). The facets are seen as an approximately linear increase in intensity. Taking account of the expected thickness dependence of the image intensity (Fig. 4) the deduced nanocrystal shape is consistent with that anticipated [46]. Such analyses will be greatly facilitated by the increased contrast and signal to noise ratio available with sub-Ångström probes, although more accurate simulations of the thickness dependence of the image contrast will be necessary.

4. Theoretical investigation of nanocrystal functionality

In this example, theory successfully elucidates the precise role of the nanoscale in imparting specific functionality to a nanostructure. Cd-rich CdSe nanocrystals below a certain critical size are efficient photo-catalysts for the fixation of CO_2, however, CdSe surfaces are not [47]. In contrast, bulk

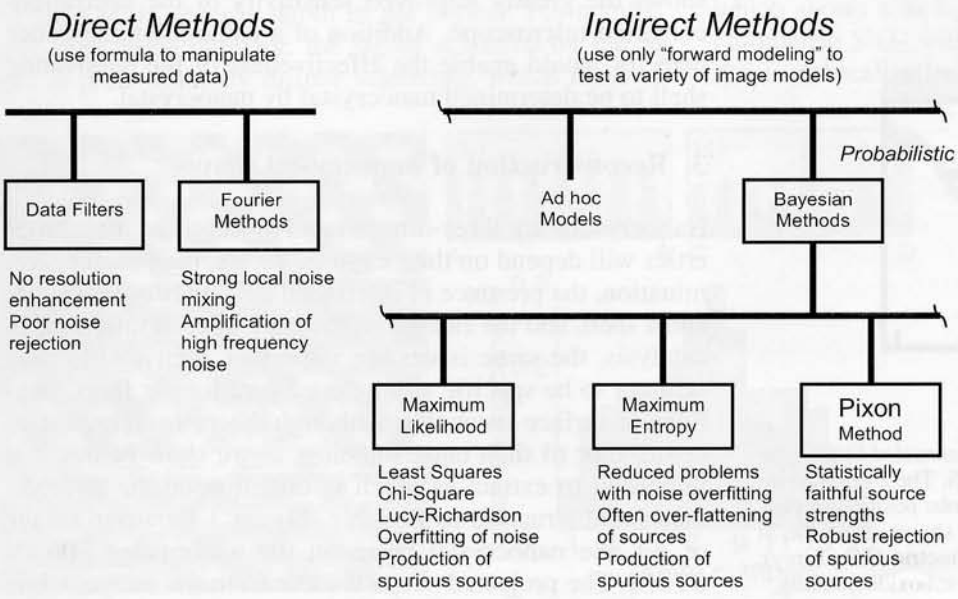

Fig. 8. Methods for image deconvolution.

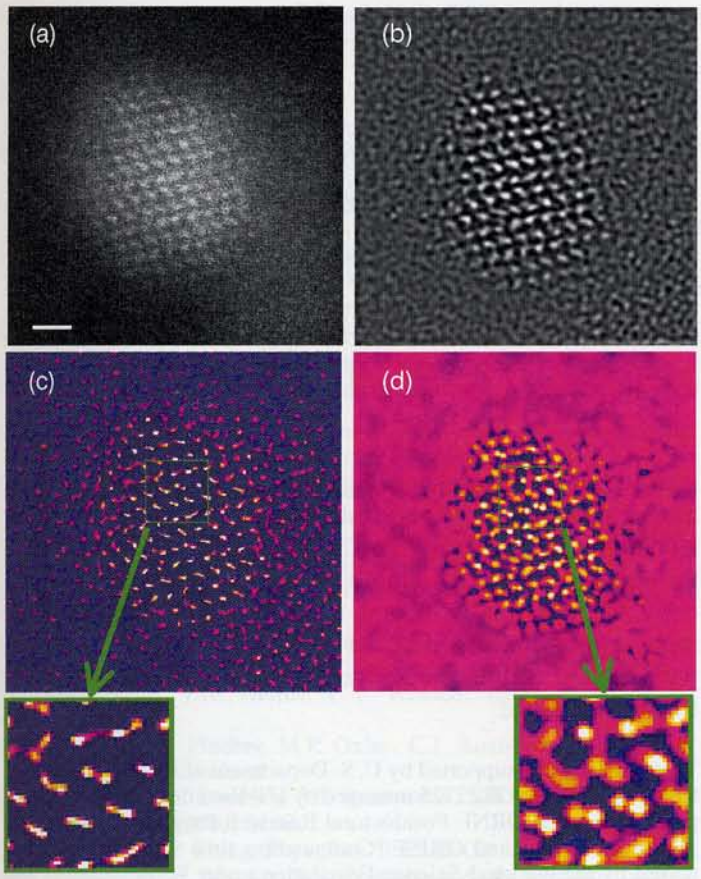

Fig. 9. (a) Raw image of a CdSe nanocrystal, (b) Fourier filtered image showing spurious detail, (c) maximum entropy reconstruction, (d) Pixon reconstruction.

CdS and ZnS surfaces do catalyze in the presence of light. First-principles calculations show that on flat stoichiometric CdSe surfaces a CO_2 molecule physisorbs and is no more reactive than in the free state. At a Cd vacancy, however, strong chemisorption occurs, and the molecule draws extra electron density from the back bonds to become negatively charged. The barrier for desorption is ≈ 0.3 eV suggesting that, even at room temperature, CO_2 molecules would be constantly chemisorbing and desorbing. If a chemisorbed molecule could desorb and carry an extra electron with it, it would be highly reactive. The energy cost is high, however, (1.3 eV, see Fig. 11a). Photoexcitation, which excites electrons to the conduction bands, is essential for the catalytic process to occur. Doping the crystal n-type in the calculation reduces the energy cost to only 0.4 eV (Fig. 11c). It is now that a nanocrystal enters the scene as an absolute necessity. The energy gap of a nanocrystal increases with decreasing size [48]. The critical diameter to enable the free flow of crystal electrons to desorbing CO_2 molecules is estimated at about 3.5 nm, which compares well with the experimental value of 5 nm. CdS and ZnS have larger bandgaps so that nanocrystals are not required.

The calculations show first, that catalysis can occur away from a surface by generation of mobile reactive species, second, that the most important role of the nanoscale is the opening of the band gap and third, that doping may avoid the need to provide light for the reaction to occur [49]. Such an understanding may assist effective implementation of semiconductor nanocrystals to alleviate global warming and the depletion of fossil fuels.

5. Anticipated performance of the 300 kV aberration-corrected STEM

The full-width-half-maximum of the probe intensity profile of the ORNL 300 kV STEM is predicted to decrease from 0.13 nm to only 0.05 nm, giving vastly greater image contrast and a dramatic improvement in signal-to-noise ratio. In crystals, the resolution of the image will no longer be limited by the incident probe, but will reach the fundamental quantum mechanical limit set by the 1s Bloch states [50] which are typically ≈ 0.05 nm in width. Spectacular improvement will also be seen for core loss EELS. Increasing the current down one selected column, and simultaneously decreasing the current illuminating surrounding columns, will improve the analytical sensitivity dramatically. Single impurity atom detection should be possible in specified columns at a grain boundary or dislocation core, with measurement of local electronic structure. This will resolve many outstanding issues in materials science: direct imaging of atomic configurations at the Si/SiO_2 interface with measurement of local electronic structure and comparison to theoretical predictions, imaging and spectroscopy of oxygen columns at electrically active grain boundaries in the cuprate superconductors and other complex oxides such

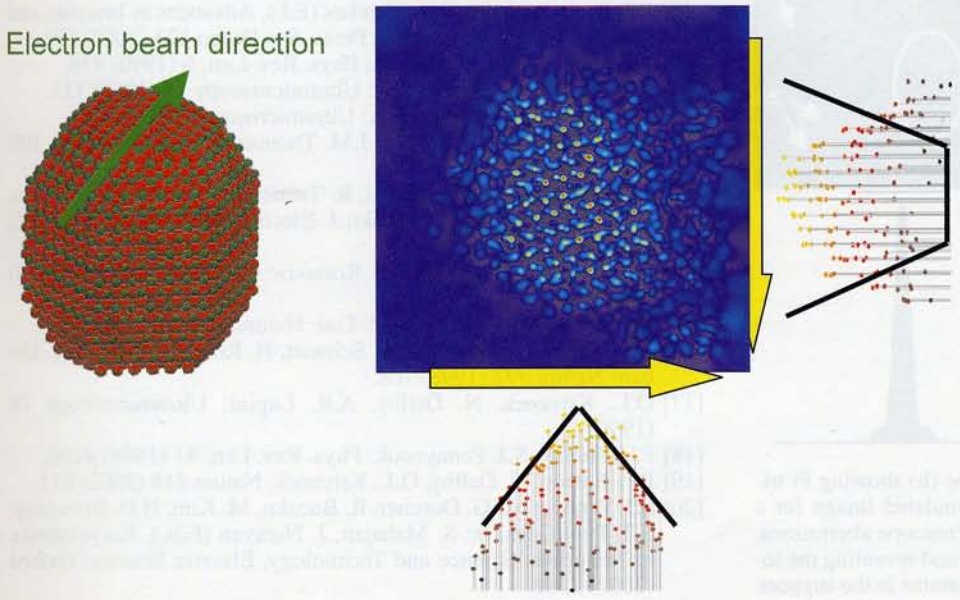

Fig. 10. Model of the expected nanocrystal shape relative to the electron beam direction with intensity plots across the Pixon reconstruction revealing facets in agreement with the model.

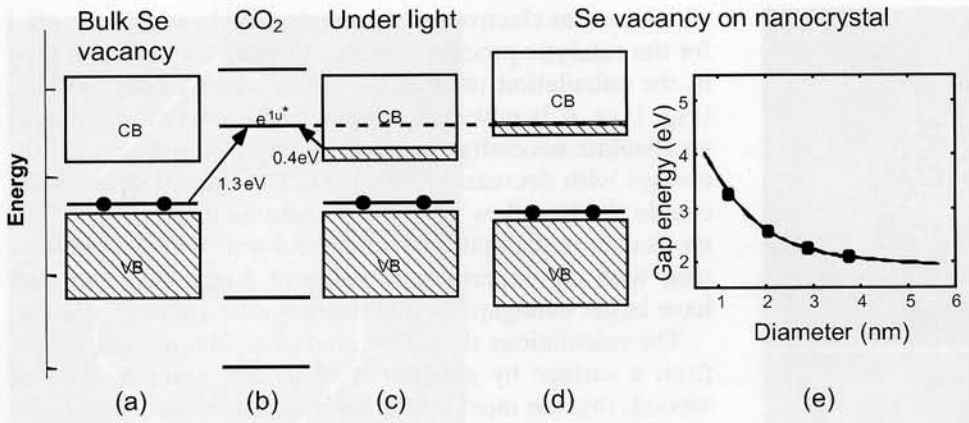

Fig. 11. Schematic showing the calculated relative energy levels of the conduction band (CB) and valence band (VB) at a Se vacancy in bulk CdSe (a) relative to the energy levels of a CO_2 molecule (b). Photoexcitation puts an electron in the conduction band, reducing the energy required to promote it to the antibonding CO_2 orbital from 1.3 to 0.4 eV (c). The additional 0.4 eV can be provided by a Se vacancy on a nanocrystal (d), due to the increase in band gap with decreasing nanocrystal size (e).

as the manganites, impurity atmospheres and localized states at dislocations and the effect on mechanical and optical properties, and for understanding the functionality of complex nanostructures.

Some of the greatest benefits may come in the field of catalysis. When a 0.13 nm beam was first achieved it became possible to see single Pt atoms on an industrial support (Fig. 12) [51]. Even such noisy images provide an ideal starting point for theoretical work. In this case, theory showed that γ-alumina is in fact a sequence of hydrogen containing compounds, the hydrogen content varying through exchange of water with the surroundings, which in turn creates surface vacancies, which in turn are the nucleation sites for the Pt trimers and dimers seen in the image [52, 53]. The dramatic improvement in image quality expected for a 0.05 nm probe is clear from the simulated image in Fig. 12, with enormously improved signal-to-noise ratio and greatly improved contrast. Direct imaging of the location of individual Pt atoms with respect to the Al^{+3} and the O^{-2} sites in the support will become possible.

Spectroscopy at the same spatial resolution will enable determination of the electronic structure at *individual sites* surrounding selected sites or clusters, for example, direct investigation of metal-support interactions and their variation from site to site. Average data can only be of limited utility in understanding industrial catalysts, which contain a large range of atomic configurations in the form of single atoms, clusters or nanocrystals, possibly including promoter atoms or poisons. The aberration-corrected STEM, through its ability for single atom imaging and spectroscopy, should finally reveal the differences between the many configurations that are present, and in combination with theory, enable the active sites and reaction pathways to be determined.

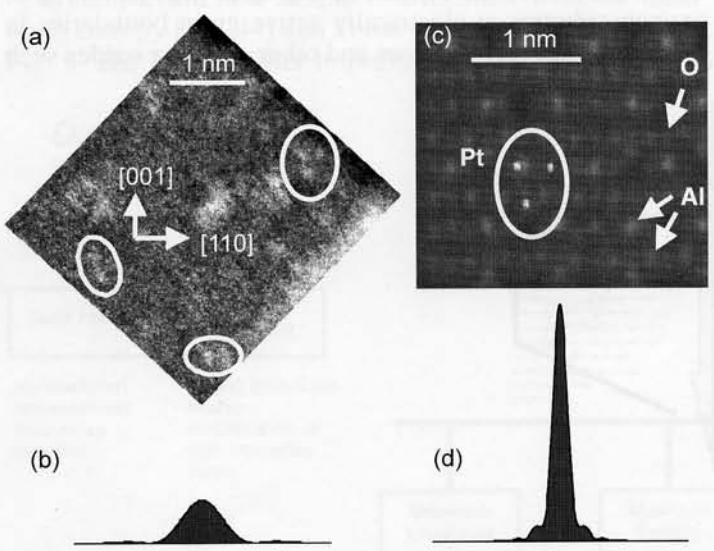

Fig. 12. (a) Z-contrast image with a 0.13 nm probe (b) showing Pt trimers and dimers on a γ-alumina support. (c) Simulated image for a 0.05 nm probe (d) expected after correction of microscope aberrations, showing greatly improved resolution and contrast, and revealing the location of the Pt atoms with respect to the Al and O atoms in the support.

This research was supported by U. S. Department of Energy under contract DE-AC05-00OR22725 managed by UT-Battelle, LLC, and by appointment to the ORNL Postdoctoral Research Program administered jointly by ORNL and ORISE. Computation time was partially supported by the National Science Foundation under DMR990002N and DMR000004N and utilized the SGI Origin 2000 at the National Center for Supercomputing Applications, University of Illinois at Urbana-Champaign.

References

[1] A.V. Crewe, J. Wall, J. Langmore: Science 168 (1970) 1338.
[2] E.M. James, N.D. Browning, A.W. Nicholls, M. Kawasaki, Y. Xin, S. Stemmer: J. Elect. Micr. 47 (1998) 561.
[3] S.J. Pennycook, P.D. Nellist, in: D.G. Rickerby, U. Valdré, G. Valdré (Eds.), Impact of Electron and Scanning Probe Microscopy on Materials Research, Kluwer Academic Publishers, Dordrecht (1999) 161.
[4] P.D. Nellist, S. J. Pennycook, in: P.W. Hawkes (Ed.), Advances in Imaging and Electron Physics, Academic Press 113 (2000) 148.
[5] N.D. Browning, M.F. Chisholm, S.J. Pennycook: Nature 366 (1993) 143.
[6] P.E. Batson: Nature 366 (1993) 727.
[7] G. Duscher, N.D. Browning, S.J. Pennycook: phys. stat. sol. (a) 166 (1998) 327.
[8] S.J. Pennycook, in: P.W. Hawkes (Ed.), Advances in Imaging and Electron Physics, Academic Press, San Diego 123 (2002) 173.
[9] S.J. Pennycook, D.E. Jesson: Phys. Rev. Lett. 6 (1990) 938.
[10] P.D. Nellist, S.J. Pennycook: Ultramicroscopy 78 (1998) 111.
[11] A.R. Lupini, S.J. Pennycook: Ultramicroscopy, (in press).
[12] M. Weyland, P.A. Midgley, J.M. Thomas: J. Phys. Chem. B 105 (2001) 7882.
[13] M. Koguchi, H. Kakibayashi, R. Tsuneta, M. Yamaoka, T. Niino, N. Tanaka, K. Kase, M. Iwaki: J. Electron Microscopy 50 (2001) 235.
[14] D.D. Perovic, A. Howie, C.J. Rossouw: Phil. Mag. Lett. 67 (1993) 261.
[15] E. Abe, S.J. Pennycook, A.P. Tsai: Nature, in press (2003).
[16] M. Haider, S. Uhlemann, E. Schwan, H. Rose, B. Kabius, K. Urban: Nature 392 (1998) 768.
[17] O.L. Krivanek, N. Dellby, A.R. Lupini: Ultramicroscopy 78 (1999) 1.
[18] P.D. Nellist, S.J. Pennycook: Phys. Rev. Lett. 81 (1998) 4156.
[19] P.E. Batson, N. Dellby, O.L. Krivanek: Nature 418 (2002) 617.
[20] S.J. Pennycook, G. Duscher, R. Buczko, M. Kim, N.D. Browning, S.T. Pantelides, in: S. Mahajan, J. Narayan (Eds.), Encyclopedia of Materials: Science and Technology, Elsevier Science, Oxford (2001) 2313.

[21] X. Fan, E.C. Dickey, P. Eklund, K.A. Williams, L. Grigorian, R.S. Buczko, S.T. Pantelides, S.J. Pennycook: Phys. Rev. Lett. 84 (2000) 4621.
[22] R. Buczko, S.J. Pennycook, S.T. Pantelides: Phys. Rev. Lett. 84 (2000) 943.
[23] M. Kim, G. Duscher, N.D. Browning, K. Sohlberg, S.T. Pantelides, S.J. Pennycook: Phys. Rev. Lett. 86 (2001) 4056.
[24] A.J. McGibbon, S.J. Pennycook, J.E. Angelo: Science 269 (1995) 519.
[25] M.M. McGibbon, N.D. Browning, M.F. Chisholm, A.J. McGibbon, S.J. Pennycook, V. Ravikumar, V.P. Dravid: Science 266 (1994) 102.
[26] M.F. Chisholm, S.J. Pennycook: Mater. Res. Soc. Bull. 22 (1997) 53.
[27] M.F. Chisholm, A. Maiti, S.J. Pennycook, S.T. Pantelides: Phys. Rev. Lett. 81 (1998) 132.
[28] Y. Yan, M.F. Chisholm, G. Duscher, A. Maiti, S.J. Pennycook, S.T. Pantelides: Phys. Rev. Lett. 81 (1998) 3675.
[29] P.M. Voyles, D.A. Muller, J.L. Grazul, P.H. Citrin, H.J.L. Gossmann: Nature 416 (2002) 826.
[30] S.J. Pennycook, D.E. Jesson: Acta Metall. Mater. 40 (1992) S149.
[31] D. VanDyck, M.O. deBeeck: Ultramicroscopy 64 (1996) 99.
[32] G.R. Anstis, D.Q. Cai, D.J.H. Cockayne: Ultramicroscopy, in press.
[33] D. Muller, J. Silcox: Ultramicroscopy 59 (1995) 195.
[34] B. Rafferty, S.J. Pennycook: Ultramicroscopy 78 (1999) 141.
[35] D.W. Essex, P.D. Nellist, C.T. Whelan: Ultramicroscopy 80 (1999) 183.
[36] L.J. Allen, S. Findlay, M.P. Oxley, C.J. Rossouw: Ultramicroscopy (2002) submitted.
[37] R. Buczko, G. Duscher, S.J. Pennycook, S.T. Pantelides: Phys. Rev. Lett. 85 (2000) 2168.
[38] S.D. Mo, W.Y. Ching: Phys. Rev. B 62 (2000) 7901.
[39] G. Duscher, R. Buczko, S. J. Pennycook et al.: Ultramicroscopy 86 (2001) 355.
[40] S.T. Pantelides, M. Ramamoorthy, S. Rashkeev, R. Buczko, G. Duscher, S.J. Pennycook, in: Y.J. Chabal (Ed.), Fundamental Aspects of Silicon Oxidation, Vol. 46, Springer-Verlag, Berlin (2001) 193.
[41] C.B. Murray, D.J. Norris, M.G. Bawendi: J. Am. Chem. Soc. 115 (1993) 8706.
[42] S.F. Gull, J. Skilling: IEE Proc. F 131 (1984) 646.
[43] P.D. Nellist, S.J. Pennycook: J. Microscopy 190 (1998) 159.
[44] A.J. McGibbon, S.J. Pennycook, D.E. Jesson: J. Microscopy 195 (1999) 44.
[45] R.C. Puetter, A. Yahil, in: D.M. Mehringer, R.L. Plante, D.A. Roberts (Eds.), Astronomical Data Analysis Software and Systems VIII, ASP, San Francisco, CA, Conf. Proc. Ser. 172 (1999) 307. http://monet.astro.uiuc.edu/adass98/Proceedings/puetterrc
[46] A.V. Kadavanich, T.C. Kippeny, M.M. Erwin, S.J. Pennycook, S.J. Rosenthal: J. Phys. Chem. B 105 (2001) 361.
[47] R.J. Stouffer, S. Manabe, K.Ya. Vinnikov: Nature 367 (1994) 634.
[48] L.W. Wang, A. Zunger: Phys. Rev. B 53 (1996) 9579.
[49] L.G. Wang, S.J. Pennycook, S.T. Pantelides: Phys. Rev. Lett. 89 (2002) 075506.
[50] S.J. Pennycook, B. Rafferty, P.D. Nellist: Microsc. Microanal. 6 (2000) 34.
[51] P.D. Nellist, S.J. Pennycook: Science 274 (1996) 413.
[52] K. Sohlberg, S.J. Pennycook, S.T. Pantelides: J. Am. Chem. Soc. 121 (1999) 7493.
[53] K. Sohlberg, S.J. Pennycook, S.T. Pantelides: J. Am. Chem. Soc. 121 (1999) 10999.

(Received November 5, 2002)

Correspondence address

S. J. Pennycook
Oak Ridge National Laboratory
Condensed Matter Sciences Division
PO Box 2008
Oak Ridge, TN 37831-6030, USA
Tel.: +1 865 574 5504
Fax: +1 865 574 4143
E-mail: pennycooksj@ornl.gov